THE JOURNAL OF BIOLOGICAL CHEMISTRY VOL. 288, NO. 31, pp. 22607–22620, August 2, 2013
Published in the U.S.A.

# Structural Changes of the Oxygen-evolving Complex in Photosystem II during the Catalytic Cycle*[S]

Received for publication, April 11, 2013, and in revised form, June 12, 2013 Published, JBC Papers in Press, June 13, 2013, DOI 10.1074/jbc.M113.476622

**Carina Glöckner**[‡], **Jan Kern**[§], **Matthias Broser**[‡], **Athina Zouni**[‡1], **Vittal Yachandra**[§2], **and Junko Yano**[§3]

*From the* [‡]*Institut für Chemie/Max-Volmer-Laboratorium für Biophysikalische Chemie, Technische Universität Berlin, D-10623 Berlin, Germany and the* [§]*Physical Biosciences Division, Lawrence Berkeley National Laboratory, Berkeley, California 94720*

**Background:** $Mn_4CaO_5$ cluster catalyzes water oxidation in photosystem II.
**Results:** Mn-Mn/Ca/ligand distances and changes in the structure of the $Mn_4CaO_5$ cluster are determined for the intermediate states in the reaction using x-ray spectroscopy.
**Conclusion:** Position of one bridging oxygen and related geometric changes may be critical during catalysis.
**Significance:** Knowledge about structural changes during catalysis is crucial for understanding the O–O bond formation mechanism in PSII.

**The oxygen-evolving complex (OEC) in the membrane-bound protein complex photosystem II (PSII) catalyzes the water oxidation reaction that takes place in oxygenic photosynthetic organisms. We investigated the structural changes of the $Mn_4CaO_5$ cluster in the OEC during the S state transitions using x-ray absorption spectroscopy (XAS). Overall structural changes of the $Mn_4CaO_5$ cluster, based on the manganese ligand and Mn-Mn distances obtained from this study, were incorporated into the geometry of the $Mn_4CaO_5$ cluster in the OEC obtained from a polarized XAS model and the 1.9-Å high resolution crystal structure. Additionally, we compared the $S_1$ state XAS of the dimeric and monomeric form of PSII from *Thermosynechococcus elongatus* and spinach PSII. Although the basic structures of the OEC are the same for *T. elongatus* PSII and spinach PSII, minor electronic structural differences that affect the manganese K-edge XAS between *T. elongatus* PSII and spinach PSII are found and may originate from differences in the second sphere ligand atom geometry.**

In nature, the water-splitting reaction takes place in photosystem II (PSII),[4] a multisubunit membrane protein in plants, algae, and cyanobacteria. This sunlight-driven reaction is catalyzed by an oxygen-evolving complex (OEC), which is located at the lumenal side of PSII. The OEC consists of four oxo-bridged manganese atoms and one calcium atom ($Mn_4CaO_5$) ligated to the D1 and CP43 subunits by carboxylate and histidine ligands (1, 2). During the oxidation of water, the OEC cycles through five different intermediate states, which are known as $S_i$ states (where $i$ ranges from 0 to 4 and refers to the oxidation equivalents stored), that couple the one-electron photochemistry of the PSII reaction center with the four-electron redox chemistry of water oxidation (Fig. 1) (3).

The geometric and electronic structural changes that occur during the catalytic cycle have been studied over the last few decades using spectroscopic methods such as electron paramagnetic resonance (EPR) spectroscopy (4), FTIR spectroscopy (5, 6), and x-ray absorption spectroscopy (XAS) (7, 8). Among them, the information regarding the geometric structural changes comes largely from extended x-ray absorption fine structure (EXAFS) studies (9, 10). The method has provided metal-to-metal (Mn-Mn and Mn-Ca) and metal-to-ligand (Mn-O/N) distances with high accuracy of ~ 0.02 Å and a distance resolution of ~0.1 Å. An important feature of this method is the possibility to control the x-ray dose by monitoring the manganese K-edge spectra. This allows data collection from the intact cluster, as the manganese ions are rapidly reduced to Mn(II), along with disruption of the cluster, when exposed to high x-ray doses normally used in protein crystallography (see below) (11–13). Various EXAFS studies, including solution EXAFS, range-extended EXAFS, and single crystal polarized EXAFS, have suggested that in the $S_1$ state there are three short Mn-Mn interactions around 2.7 Å, one long Mn-Mn interaction at around 3.3 Å, and three to four Mn-Ca interactions (based on strontium XAS studies (14, 15)) at around 3.4–3.9 Å. The combination of polarized EXAFS data from single crystals of dimeric PSII core complexes (PSIIcc) with x-ray diffraction (XRD) data (16) led to three proposed models for the $Mn_4CaO_5$ cluster (17), one of which is shown in Fig. 2.

However, due to the limited knowledge about the accurate geometry of the $Mn_4Ca$ cluster, a direct correlation of the spec-

* This work was supported, in whole or in part, by National Institutes of Health Grant GM55302. This work was also supported by Department of Energy, Director of the Office of Science, Office of Basic Energy Sciences, Division of Chemical Sciences, Geosciences, and Biosciences, Contract DE-AC02-05CH11231 and Deutsche Forschungsgemeinschaft (within the framework of the Center of Excellence on Unifying Concepts in Catalysis) Project B1, coordinated by the Technische Universität Berlin, Sfb 498, Project C7, and Sfb 1078, Project A5 (to A. Z.).
[S] This article contains supplemental Table 1.
[1] To whom correspondence may be addressed: Institut für Chemie/Max-Volmer-Laboratorium für Biophysikalische Chemie, Technische Universität Berlin, Strasse des 17. Juni 135, D-10623 Berlin, Germany. E-mail: zouni@mailbox.tu-berlin.de.
[2] To whom correspondence may be addressed: Physical Biosciences Division, Lawrence Berkeley National Laboratory, MS 66-0200, 1 Cyclotron Rd., Berkeley, CA 94720-8099. Tel.: 510-486-4963; E-mail: vkyachandra@lbl.gov.
[3] To whom correspondence may be addressed: Physical Biosciences Division, Lawrence Berkeley National Laboratory, MS 66-0200, 1 Cyclotron Rd., Berkeley, CA 94720-8099. Tel.: 510-486-4366; E-mail: jyano@lbl.gov.
[4] The abbreviations used are: PSII, photosystem II; EXAFS, extended x-ray absorption fine-structure spectroscopy; FT, Fourier-transform; OEC, oxygen-evolving complex; PSIIcc, photosystem II core complex; XANES, x-ray absorption near-edge spectroscopy; XAS, x-ray absorption spectroscopy; XRD, x-ray diffraction.



This is an Open Access article under the CC BY license.

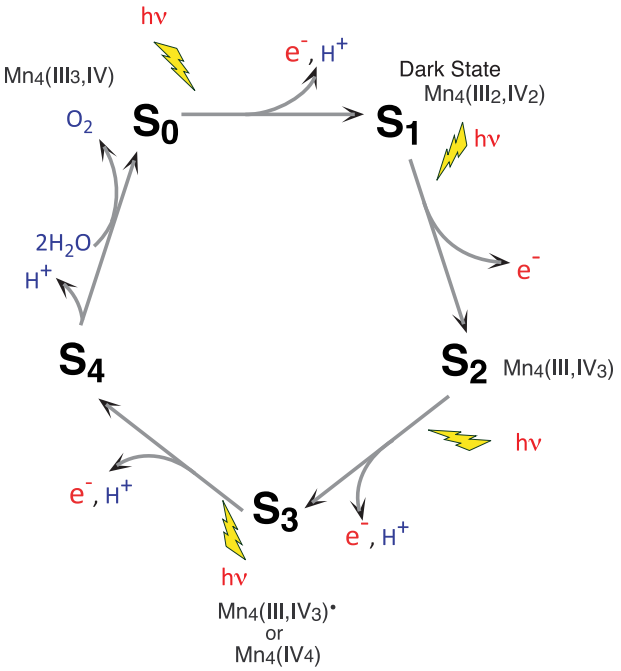


FIGURE 1. **Kok cycle.** The classical Kok cycle with the intermediate S states in water oxidation is shown. Proposed oxidation states for the manganese atoms are indicated. Electron and proton transfers are illustrated in *red* and *blue*, respectively.

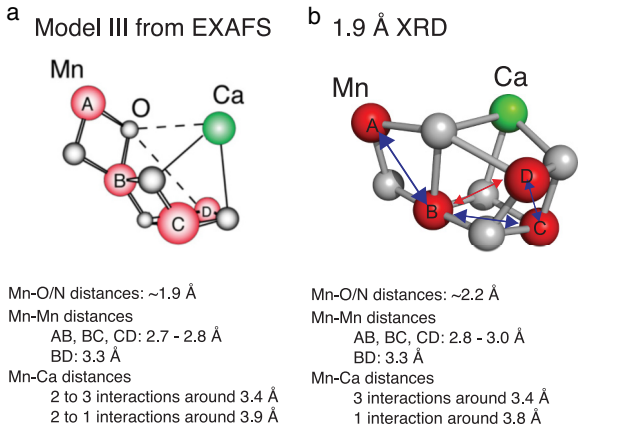


FIGURE 2. **Structural models for the $Mn_4CaO_5$ cluster.** The structural models for the $Mn_4CaO_5$ cluster from (*a*) the polarized EXAFS and strontium EXAFS studies (15, 17) and (*b*) the 1.9 Å resolution XRD study (1) are shown. The Mn-Mn and Mn-O/N ligand distances from each of these studies are summarized below the respective structural model. Manganese atoms are depicted in *red* and calcium in *green*.

troscopic data to structural changes of the cluster is difficult. The recent high resolution crystal structure from XRD reported by Umena *et al.* (1) has provided a more precise geometry of the OEC structure with possibly limited effects from radiation damage (see below). This high resolution XRD structure has clearly located one calcium and four manganese positions facilitating the determination of the overall geometry of the metal cluster. Although the similarities in the number of Mn-Mn and Mn-Ca vectors are striking between the XRD and EXAFS structural models, there are distinct differences in the distances as shown in Fig. 2. The major differences are in the Mn-Mn and Mn-O distances, which are longer by 0.1–0.2 Å for the Mn-Mn and ~ 0.3 Å for the Mn-O distances than determined by x-ray spectroscopy methods. We speculate that these differences in distances, summarized in Fig. 2, are caused by radiation damage during the XRD data collection and thus lead to some of the differences in the proposed models for the clusters.

Nevertheless, the 1.9 Å resolution structure of PSIIcc from *Thermosynechococcus vulcanus* serves as a new basis to relate our spectroscopic data with the structural changes that occur during the catalytic $S_i$ state transitions.

Until now, most of the XRD studies were performed with crystals of PSIIcc purified from the thermophilic cyanobacteria *Thermosynechococcus elongatus* and *T. vulcanus*, whereas spinach thylakoid membranes were used for most of the EXAFS studies. The polarized EXAFS studies of the S1 state were carried out using crystals from *Thermosynechococcus elongatus* (17). Although a crystallographic model of PSIIcc from spinach is still missing, PSIIcc x-ray structures from cyanobacteria are available for its dimeric (1, 16, 18–21) as well as its monomeric form (22).

In this study, structural changes of the $Mn_4CaO_5$ cluster through the $S_0$ to $S_3$ states were analyzed by means of EXAFS using the same dimeric PSIIcc preparations from *T. elongatus* as used for crystallography. The EXAFS parameters obtained from the $S_1$ state are incorporated into the analysis of other S states with the same data treatment methods, and possible structural changes are proposed based on the geometry obtained from the 1.9 Å resolution crystal structure (1).

To investigate possible differences regarding the organization of the $Mn_4CaO_5$ cluster between various PSII samples, we additionally compared our EXAFS data of the S1 state from dimeric PSIIcc samples with data obtained from monomeric PSIIcc samples and from spinach thylakoid membrane fragments.

## EXPERIMENTAL PROCEDURES

*Sample Preparation*—The preparation of monomeric and dimeric PSIIcc solutions from *T. elongatus* followed the protocol by Kern *et al.* (23). Note that the PSII monomer fraction was not further purified in a third chromatography step as described in Broser *et al.* (22). The PSIIcc monomer and dimer solutions in 100 mM MES, pH 6.5, 5 mM $CaCl_2$, 0.015% $\beta$-dodecyl maltoside were concentrated to about 15 mM chlorophyll *a* and slowly mixed with 100% glycerol to a final concentration of 40% glycerol and 10 mM chlorophyll *a*.

*Sample Illumination*—A frequency-doubled (532 nm) Nd:YAG laser was used (8-ns pulse width) for flash illumination. To maintain maximal synchronization of the PSII centers on flash illumination, the fast recombination reaction between both the $S_2$ and $S_3$ states and the reduced form of the redox-active tyrosine residue $Tyr_D$ must be suppressed. This was achieved by the application of one pre-flash, followed by a 60-min dark adaptation period at room temperature. This procedure synchronizes the PSII centers into predominantly the $S_1Y_D^{ox}$ state. Immediately before flashing, the electron acceptor was added to the sample (1 $\mu$l of 50 mM 2-phenyl-*p*-benzoquinone in MeOH per 40 $\mu$l of sample). Each sample was then given 0 or 1–6 flashes at room temperature (0F, 1F, 2F, 3F, 4F, 5F, and 6F samples), with intervals of 1.0 s between the individ-

ual flashes. The light was focused on the sample by using cylindrical lenses. After the last flash, the samples were frozen immediately (within 1 s) in liquid nitrogen. The EPR spectra were collected, and the samples were stored at 77 K for further use in the XAS experiments.

*EPR Spectroscopy*—Low temperature X-band EPR spectra were recorded by using a Varian E109 EPR spectrometer equipped with a model 102 microwave bridge. For the $S_2$ state multiline-signal measurements (data not shown), the sample temperature was maintained at 8 K with the use of an Air Products LTR liquid helium cryostat. Spectrometer conditions were as follows: microwave frequency, 9.21 GHz; field modulation amplitude, 32 G at 100 kHz; microwave power, 30 milliwatts. EPR multiline-signal amplitudes were quantified by adding peak-to-trough amplitudes of the hyperfine lines down field from g = 2. For each sample (0–6F), the designated $S_2$ state multiline EPR signal peaks were normalized by using the amplitude of the $Fe^{III}$ signal at g = 4.3 as an internal reference (data not shown).

We used the Kok model (Fig. 1) as described in Messinger *et al.* (24) to calculate the S state population for each flash number (Table 1) and have compared the calculated $S_2$ state values (normalized to be 100% for 1F amplitude) to the normalized amplitudes. The error between the calculated and measured $S_2$ state populations was minimized. Because of factors such as redox equilibrium between the cofactors in PSII, it is inevitable that some dephasing occurs, although the OEC is advanced through the various S states. The possibility of double hits and miss hits as introduced by the original Kok model (3) was considered in the S state population analysis.

*XAS Data Collection*—X-ray absorption spectra were collected at the Stanford Synchrotron Radiation Lightsource on beamline 7-3 at an electron energy of 3.0 GeV and an average current of 300 mA. The intensity of the incident x-rays was monitored by a $N_2$-filled ion chamber ($I_0$) in front of the sample. The radiation was monochromatized by an Si(220) double crystal monochromator. The total photon flux on the sample was limited to $1 \times 10^7$ photons/$\mu m^2$, which was determined to be nondamaging on the basis of detailed radiation-damage studies of PSIIcc solution samples (12). The samples were protected from the beam during spectrometer movements between different energy positions by a shutter synchronized with the scan program. The samples were kept at 8 K in a helium atmosphere at ambient pressure by using an Oxford CF-1208 continuous-flow liquid helium cryostat. Data were recorded as fluorescence excitation spectra by using a germanium 30-element energy-resolving detector (Canberra Electronics). For manganese XAS, energy was calibrated by the pre-edge peak of $KMnO_4$ (6543.3 eV), which was placed between two $N_2$-filled ionization chambers ($I_1$ and $I_2$) after the sample.

The method for collecting XANES and EXAFS spectra as a function of x-ray dose is described in Ref. 12.

*EXAFS Curve Fitting Procedures*—Curve fitting was performed with Artemis and IFEFFIT software using *ab initio*-calculated phases and amplitudes from the program FEFF 8.2 (25, 26). These *ab initio* phases and amplitudes were used in the EXAFS Equation 1,

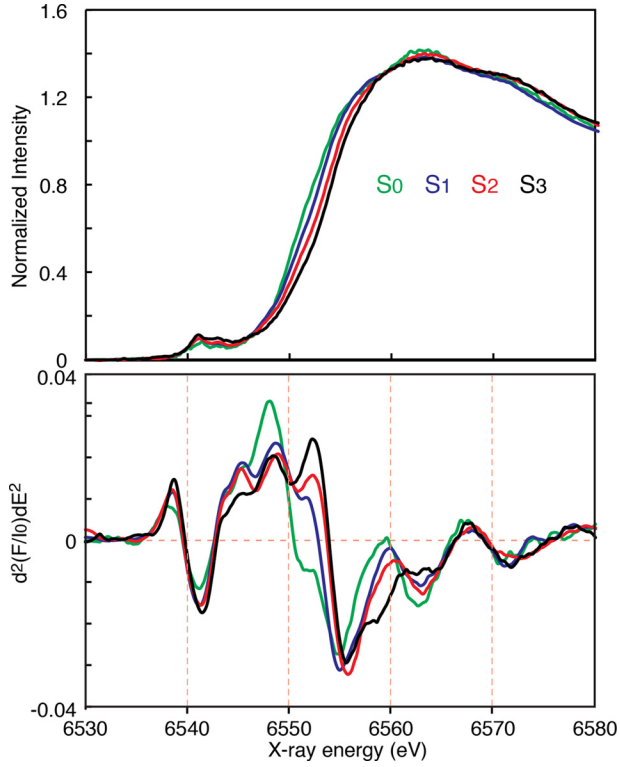


FIGURE 3. **XANES spectra of dimeric PSIIcc solution in the $S_0$, $S_1$, $S_2$, and $S_3$ states.** Manganese XANES (*top*) and their second derivative spectra (*bottom*) of dimeric PSIIcc solution in the $S_0$ (*green*), $S_1$ (*blue*), $S_2$ (*red*), and $S_3$ (*black*) states are shown. The zero-crossing energy of the second derivative spectra are 6550.94 eV for $S_0$, 6553.45 eV for $S_1$, 6554.12 eV for $S_2$, and 6554.40 eV for $S_3$.

$$\chi(k) = S_0^2 \sum_j \frac{N_j}{kR_j^2} f_{\mathrm{eff}j}(\pi,k,R_j) e^{-2\sigma_j^2 k^2} e^{-2R_j/\lambda_j(k)} \sin(2kR_j + \phi_{ij}(k)) \quad \text{(Eq. 1)}$$

The neighboring atoms to the central atom(s) are divided into $j$ shells, with all atoms with the same atomic number and distance from the central atom grouped into a single shell. Within each shell, the coordination number $N_j$ denotes the number of neighboring atoms in shell $j$ at a distance of $R_j$ from the central atom. $f_{\mathrm{eff}j}(\pi,k,R_j)$ is the *ab initio* amplitude function for shell $j$, and the Debye-Waller term $e^{-2\sigma j2k2}$ accounts for damping due to static and thermal disorder in absorber-backscatterer distances. The mean free path term $e^{-2Rj/\lambda j(k)}$ reflects losses due to inelastic scattering, where $\lambda_j(k)$ is the electron mean free path. The oscillations in the EXAFS spectrum are reflected in the sinusoidal term, $\sin(2kR_j + \varphi_{ij}(k))$ where $\varphi_{ij}(k)$ is the *ab initio* phase function for shell $j$. ${S_0}^2$ is an amplitude reduction factor due to shake-up/shake-off processes at the central atom(s). The EXAFS equation was used to fit the experimental data using $N$, $R$, and the EXAFS Debye-Waller factor ($\sigma^2$) as variable parameters.

## RESULTS

*XANES of PSIIcc Dimer, $S_0$ to $S_3$ States*—Fig. 3 shows the XANES spectra of dimeric PSIIcc solutions from $S_0$ to $S_3$ states. Pure S state spectra were obtained by deconvoluting the spectra of flash samples (0–3F) using the S state distributions obtained

**TABLE 1**
**S state population of flashed samples (unit, %)**

| No. of flashes | $S_0$ | $S_1$ | $S_2$ | $S_3$ |
|---|---|---|---|---|
| 0 | 3.0 | 88.0 | 9.0 | 0.0 |
| 1 | 0.3 | 11.5 | 80.1 | 8.1 |
| 2 | 6.9 | 2.8 | 28.4 | 61.8 |
| 3 | 52.9 | 7.5 | 15.7 | 23.9 |

from EPR spectroscopy (Table 1). The overall trend of the XANES edge shift is similar to that reported from spinach thylakoid membrane preparations (24). The edge position shifts to higher energy during the $S_0$ to $S_3$ transitions. The zero-crossing energies of the rising edge spectrum, which are often used as an indicator of the oxidation state, are 6550.94 eV for $S_0$, 6553.45 eV for $S_1$, 6554.12 eV for $S_2$, and 6554.40 eV for $S_3$.[5]

*EXAFS of PSIIcc Dimer, $S_0$ to $S_3$ States*—The $k^3$-weighted EXAFS spectra and its Fourier-transformed (FT) spectra of dimeric PSIIcc solutions in the $S_0$ to $S_3$ states are shown in Fig. 4. The phase and amplitude of the $k^3$-weighted spectra change during the S state transitions (Fig. 4*a*). Particularly, an increase in the EXAFS oscillation frequency is visible in the $S_2$ to $S_3$ transition at higher *k*-space values, suggesting the increase in some of the predominant scatterer-backscatterer distances during this transition. This increased oscillation frequency was also reported in the earlier EXAFS study by Liang *et al.* (27) using spinach thylakoid membrane fragments.

In the FT spectra (Fig. 4*b*), the positions of the three peaks labeled I to III correspond to the shells of scatterers at different apparent distances from the manganese absorber; the FT peak I is from the manganese-ligand interactions at ~1.9 Å; peak II is mainly from di-$\mu$-oxo-bridged Mn-Mn interactions (~2.7 Å), and peak III is from mono-$\mu$-oxo-bridged Mn-Mn (~3.3 Å) as well as from Mn-Ca interactions (~3.4 Å). Upon the $S_0$ to $S_1$ state transition, peaks I and II are shifted toward shorter apparent distances. This suggests a shortening of the manganese-ligand and the Mn-Mn distances. The $S_1$ to $S_2$ state transition does not show a detectable peak shift, although the peak intensity increases in peak I as well as peak II. The $S_2$ to $S_3$ state transition is accompanied by more substantial spectral changes; the FT peak II shifts to longer distance and the peak III region splits into two. Then, upon $S_3$ to $S_0$ state transition, peak II shifts to shorter distance and peak III goes back to a single peak.

*EXAFS Curve Fitting Results of PSIIcc Dimer, $S_0$ to $S_3$ States*—Manganese EXAFS curve fits were carried out for the $k^3$-weighted EXAFS spectra of the dimeric PSIIcc solutions in the $S_0$ to $S_3$ states. Table 2 summarizes the curve fitting parameters, in which *R*, *N*, and $\sigma^2$ are the actual distance, coordination number, and EXAFS Debye-Waller factor (in Å$^2$), respectively. *N* values are defined as the total number of absorber-backscatter vectors divided by the number of absorber atoms per OEC. The *R* factor ($R_f$, in %) shows the goodness of the fit.

The ~3.4-Å Mn-Ca EXAFS peak in manganese XAS is concealed by the presence of the Mn-Mn interaction around ~3.3 Å in the peak III region. Hence, it would be ideal to carry out calcium XAS on each S state, to obtain detailed information about the Mn-Ca interactions. However, it is challenging to collect calcium XAS on PSII due to the following: (*a*) the difficulties of avoiding calcium contamination during sample preparation and data collection, and (*b*) the higher absorption coefficient of calcium at its absorption energy (4050 eV) as compared with the strontium K-edge energy (16,200 eV) that leads to faster radiation damage. Therefore, we used the information of strontium EXAFS changes previously obtained from strontium-substituted *T. elongatus* (15) to estimate the distances and the number of Ca-Mn interactions that contribute to the manganese EXAFS in the peak III region.

The best fits are shown in Fig. 5 and the fitting parameters are summarized in Table 2 (for the detailed EXAFS fit, see supplemental Table 1).

*$S_1$ State*—As was shown in previous studies with spinach thylakoid membrane fragments and *Synechocystis* PSII $S_1$ state (28), the predominant feature of the EXAFS spectrum of the PSII $S_1$ state arises from about six manganese-ligand interactions at an average distance of 1.87 Å, three di-$\mu$-oxo-bridged Mn-Mn interactions at ~2.7 Å, and one longer Mn-Mn interaction around 3.3 Å. In addition, there are two to three Mn-Ca interactions at 3.4 Å, which is confirmed by calcium XAS (29) as well as strontium XAS on strontium-substituted PSIIcc and PSII membranes (15, 30). In this study, one shell fit to the peak II region shows an average Mn-Mn distance of 2.73 Å, although two shell fits prefer two distances at 2.71 and 2.79 Å with a slight improvement in the fit quality (supplemental Table 1 and Fig. 5*b*). We note that the small distance heterogeneity in the Mn-Mn interactions within 2.7 to 2.8 Å (peak II) cannot be justified based only on our current conventional EXAFS data due to the limited distance resolution. We, however, used two shell fits in this study as such distance heterogeneity has been reported in the $S_0$ state and polarized EXAFS spectra of the $S_1$ state (17, 28, 31). Moreover, the range-extended EXAFS studies have provided evidence for the presence of distance heterogeneity (28, 31).

In the previous strontium XAS study on strontium-substituted PSIIcc (15), the data showed that there are two types of Sr-Mn interactions, one around 3.5 Å and the other around 3.8 Å. However, the exact ratio of these interactions was inconclusive. Just recently, Koua *et al.* (32) published a structural model of the $Mn_4SrO_5$ cluster in strontium-substituted PSIIcc from *T. vulcanus* at 2.1 Å resolution. The model shows two Sr-Mn interactions at 3.5 Å, one at 3.6 Å and one at 4.0 Å. Taking the estimated standard uncertainty of 0.21 Å into account, these results argue for a 3:1 ratio for short to long Sr-Mn interactions. In this study, both a 2:2 or a 3:1 ratio for the two distances of the Ca-Mn interactions were tested, and only subtle differences were observed in the $R_f$ value (Table 2). This trend is true for all the S states described below.

*$S_2$ State*—The starting parameters for the $S_2$ state EXAFS fit were taken from the best fits of the $S_1$ state. A shortening of the

[5] Note that several methods have been used for assigning the formal oxidation states of metals using XANES, which includes the half-height energy of the edge jump, white line energy of the edge, as well as the zero-crossing energy of the XANES 2nd derivative spectra. None of these are perfect methods for studying the charge density changes of metals. However, the zero-crossing energy seems to be the most reliable qualitative method, when the energy shift is accompanied by spectral shape changes. This is based on XANES studies on various model complexes.

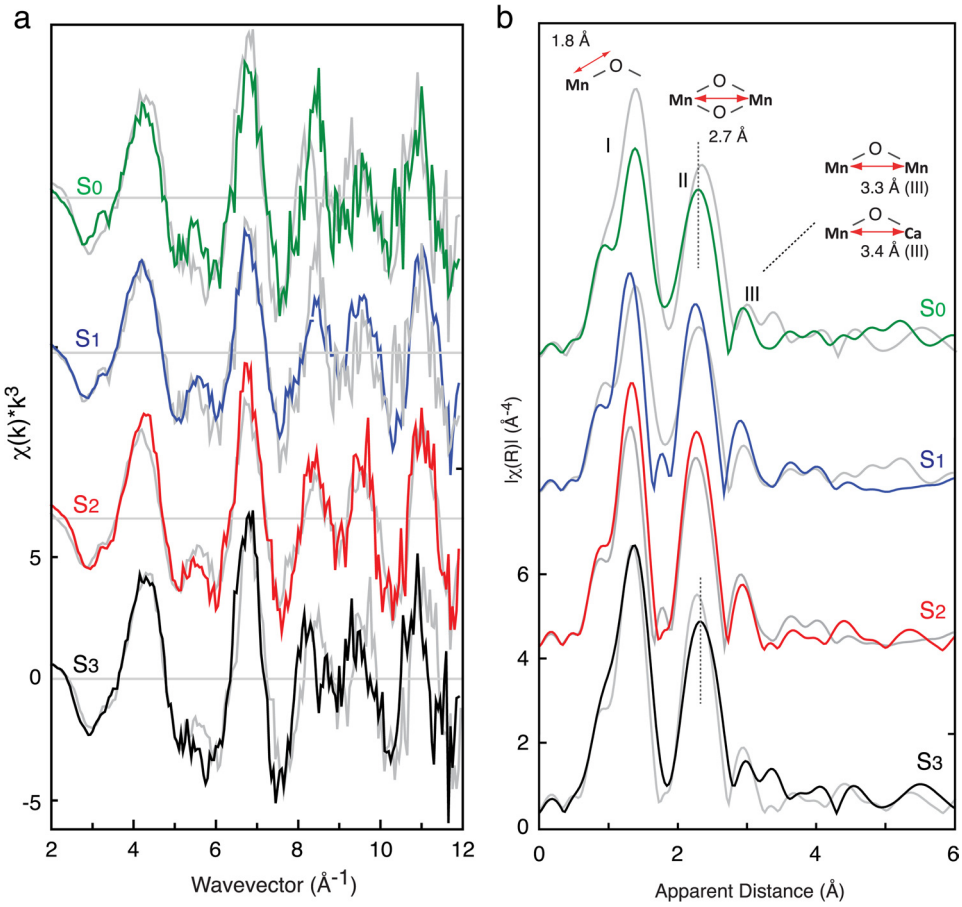


FIGURE 4. **EXAFS and FT spectra of dimeric PSIIcc solutions in the $S_0$, $S_1$, $S_2$, and $S_3$ states.** *a*, $k^3$-weighted EXAFS spectra; *b*, their Fourier-transformed spectra of dimeric PSIIcc solution in the $S_0$ (*green*), $S_1$ (*blue*), $S_2$ (*red*), and $S_3$ (*black*) states are shown. For comparison, the spectrum of the $S_{n-1}$ state is overlaid in the $S_1$, $S_2$, and $S_3$ spectra (*gray*). Prominent changes between the $S_2$ and the $S_3$ state and the $S_3$ and the $S_0$ state in the peak II of the FT spectra are indicated by a *dashed line*. All spectra are shown in the same scale but with a vertical offset.

Mn-Mn distances was observed in the $S_1$ to $S_2$ state transition. In the $S_2$ state, the three Mn-Mn distances around 2.7 Å (peak II) become more homogeneous, which is evident by the stronger peak II with a lower Debye-Waller factor. When the two shell fits were applied for peak II, the two distances are closer (2.72 and 2.75 Å), which is within the precision limit (~0.02 Å) of the conventional manganese EXAFS measurements. The one shell fit for the peak II region showed the average Mn-Mn distances to be 2.74 Å (Fig. 5*c* and Table 2). This result suggests that one longer Mn–Mn bond at 2.79 Å in the $S_1$ state becomes shorter in the $S_2$ state due to the oxidation state change of manganese from Mn(III) to Mn(IV).

*$S_3$ State*—As shown in Fig. 4, we see substantial spectral changes in the $S_2$ to $S_3$ state transition, particularly in the peak III region. Also, the intensity of peak II is weaker than in the $S_2$ state. Therefore, we have tested two possible structural models as follows: case a has a similar geometry to the $S_1$ and the $S_2$ states with three di-$\mu$-oxo-bridged Mn-Mn units (~2.7 Å, $n = 1.5$) and a longer mono-$\mu$-oxo-bridged Mn-Mn unit (~3.2 Å, $n = 0.5$), and case b has four di-$\mu$-oxo bridges (~2.7 Å, $n = 2$) and no mono-$\mu$-oxo bridge. In case a, the best fit results for the $S_1$ state were used as starting parameters. The larger peak II width as compared with the $S_2$ state is reflected in the increased distance heterogeneity. In the one-shell fit (supplemental Table 1), the average Mn-Mn distance increased from 2.74 to 2.76 Å. When a two shell fit was applied, the fit quality improved with two Mn-Mn distances of 2.75 and 2.79 Å (Table 2 and supplemental Table 1). In case b, we assumed all manganese being connected by at least two oxo bridges. The fit quality was slightly better in case a (supplemental Table 1). Upon a simple manganese oxidation reaction, we expect a shortening of Mn-Mn interactions due to the elimination of Jahn-Teller distortion in Mn(III). Therefore, the increased Mn-Mn distances observed in both models ($S_3$ fit case a and fit case b) imply that in the $S_2$ to $S_3$ state transition, the structural changes we observe are not simply due to the distance change that is accompanied by the oxidation state change, but it is rather due to a fundamental geometrical change. Possible reasons for such an elongation are described under "Discussion."

*$S_0$ State*—Upon $S_3$ to $S_0$ state transition, the OEC goes from the most oxidized state to the most reduced state in the catalytic cycle. We observe a decrease of peak I and II intensities as well as a shortening of the average peak II distance. When two shell fits were applied, we see two Mn-Mn distances around 2.77 Å and one short distance at 2.68 Å. This 1:2 (2.7:2.8 Å) ratio is different from the results reported by Robblee *et al.* (33) using spinach thylakoid membrane fragments (ratio of 2:1). This difference could be due to the improved fitting protocol employed in this study.

**TABLE 2**
**EXAFS fit table for each S state**

$k = 2.4–11.3$ (Å$^{-1}$), $E_0 = 6561.30$ eV, and $S_0^2 = 0.85$. The boldface letters show the fixed parameters. The $\sigma^2$ values of shorter Mn-O and longer Mn-O/Mn-N interactions were linked and assumed to be the same (shown in italic letters). In the same manner, the $\sigma^2$ values of ~2.7 Å Mn-Mn and ~2.8 Å Mn-Mn interactions were linked. The numbers in parentheses show the results when the *N* ratio of the shorter *versus* longer Mn-Ca interactions is fixed to 0.75:0.25.

| | $S_0$ | | | $S_1$ | | | $S_2$ | | | $S_3$_fitA | | | $S_3$_fitB | | |
|---|---|---|---|---|---|---|---|---|---|---|---|---|---|---|---|
| Path | R | N | $\sigma^2$ | R | N | $\sigma^2$ | R | N | $\sigma^2$ | R | N | $\sigma^2$ | R | N | $\sigma^2$ |
| MnO | 1.91 | 4.5 (4.4) | *0.009* | 1.86 | 3.9 | *0.005* | 1.86 | 4.1 | *0.006* | 1.84 (1.88) | 3.5 (6.0) | *0.005 (0.009)* | 1.85 | 3.8 | *0.004* |
| MnO/N | 2.26 | 1.5 (1.6) | *0.009* | 2.05 | 2.1 | *0.005* | 2.02 | 1.9 | *0.006* | 1.97 (2.14) | 2.5 (0.0) | *0.005 (0.009)* | 1.99 (2.00) | 2.2 (2.1) | *0.004* |
| MnMn | 2.68 | **0.5** | *0.002* | 2.71 | **1.0** | *0.002* | 2.74 | **1.5** | 0.002 | 2.75 | **1.0** | *0.002* | 2.72 (2.76) | **1.0** | *0.002 (0.003)* |
| MnMn | 2.77 | **1.0** | *0.002* | 2.79 | **0.5** | *0.002* | | | | 2.79 (2.78) | **0.5** | *0.002* | 2.82 (2.78) | **1.0** | *0.002 (0.003)* |
| MnMn | 3.30 | **0.5** | 0.007 | 3.28 (3.27) | **0.5** | 0.002 (0.003) | 3.30 | **0.5** | 0.005 | 3.26 | **0.5** | 0.002 | | | |
| MnC[a] | 3.05 (3.04) | **1.5** | 0.005 | 2.99 (3.00) | **1.5** | 0.005 | 2.99 | **1.5** | 0.005 | 2.96 | **1.5** | 0.005 | 3.58 (2.96) | **1.5** | 0.005 |
| MnCa | 3.36 | **0.5 (0.75)** | 0.007 | 3.36 | **0.5 (0.75)** | 0.007 | 3.36 | **0.5 (0.75)** | 0.007 | 3.37 (3.36) | **0.5 (0.75)** | 0.007 (0.009) | 3.34 (3.31) | **0.5 (0.75)** | 0.002 |
| MnCa | 3.99 | **0.5 (0.25)** | 0.015 | 3.99 | **0.5 (0.25)** | 0.008 | 3.99 | **0.5 (0.25)** | 0.008 | 3.99 | **0.5 (0.25)** | 0.009 (0.015) | 3.99 | **0.5 (0.25)** | 0.009 |
| MnO[a] | 3.34 | **2.5** | 0.015 | 3.14 | **2.5** | 0.091 (0.085) | 3.14 | **2.5** | 0.086 | 3.06 | **2.5** | 0.015 | 3.08 (3.06) | **2.5** | 0.015 |
| *R* factor | 3.5% (3.7%) | | | 1.8% (2.0%) | | | 2.8% (2.6%) | | | 2.6% (2.7%) | | | 4.5% (3.1%) | | |
| | $\Delta E = -7.2$ (−6.8) | | | $\Delta E = -9.8$ (−9.5) | | | $\Delta E = -8.0$ (−8.3) | | | $\Delta E = -8.8$ (−9.6) | | | $\Delta E = -7.9$ (−7.1) | | |

[a] Mn-C interactions (Mn to C of carboxylates) and Mn-O interactions (Mn to O of carboxylates) were included in the fit, although their contribution is minor.

*Comparison of the $S_1$ State of T. elongatus Dimeric and Monomeric PSIIcc and Spinach PSII*—A comparison of the XAS spectra of all three types of PSII samples in the dark stable $S_1$ state is shown in Fig. 6. Although the XANES region (Fig. 6*a*) for the PSIIcc dimer and monomer samples are identical, the XANES spectrum of spinach PSII thylakoid membrane fragments shows slight differences to that of PSIIcc (Fig. 6*a*), which become more pronounced in the 2nd derivative spectrum (Fig. 6*a*, *bottom panel*). PSIIcc dimer/monomer as well as spinach PSII thylakoid membrane fragments show almost identical EXAFS spectra (Fig. 6*b*), confirming that the $Mn_4CaO_5$ cluster has the same structure.

*Radiation Damage of the $S_1$ State of Dimeric PSIIcc*—Solutions of dimeric PSIIcc were exposed to various x-ray doses at 100 K, leading to reduction of 5, 10, or 25%, respectively, of the manganese in the sample from Mn(III,IV) to Mn(II). The corresponding XANES and EXAFS spectra (recorded at 8 K) are shown in Fig. 7. A clear shift in the K-edge toward lower energies, due to the reduction of manganese to Mn(II), can be seen in Fig. 7*a* when compared with the $S_1$ state spectrum. The amplitudes of the $k^3$-weighted spectra change drastically with increasing manganese reduction (Fig. 7*c*), and the oscillations are more damped compared with the $S_1$ state. In the *k*-range 8–11.5 Å$^{-1}$, a dephasing is clearly visible, especially at 10 and 25% damage compared with the $S_1$ state. Also, the pronounced oscillation in the range of $k = 6–8$ Å$^{-1}$ is reduced in amplitude in all spectra of the damaged PSIIcc solutions compared with the $S_1$ state spectrum. In the FT spectra (Fig. 7*b*), the intensities of all three peaks are decreased upon higher manganese reduction, with the most pronounced decrease in the peak II intensity. EXAFS curve fitting results (Table 3) show that upon increased manganese reduction the number of shorter Mn-Mn interactions are reduced and the number of longer Mn-Mn interactions are increased.

## DISCUSSION

*XANES Changes, $S_0$ to $S_3$ States*—In this study with *T. elongatus* PSII core preparations, we observed a similar trend in the XANES energy shift to that seen for the spinach thylakoid membrane fragments (24). The similarity of the K-edge XANES between the cyanobacterial and spinach PSII suggests that the oxidation states proposed for spinach (for example, $Mn_2^{III}Mn_2^{IV}$ for the $S_1$ state) are also valid for the cyanobacterial preparations. The previous study by Messinger *et al.* (24) showed that manganese oxidation occurs during the $S_0$ to $S_1$ and $S_1$ to $S_2$ state transitions based on the 1–2 eV XANES energy shifts. A much smaller shift was observed during the $S_2$ to $S_3$ state transition that is accompanied by a change in the edge shape, similar to that shown in Fig. 3 for cyanobacterial PSII. The interpretation was that the chemical changes during the $S_2$ to $S_3$ state transition are not the same as the ones during the $S_0$ to $S_1$ and $S_1$ to $S_2$ state transitions. One possible explanation for this was that a unit other than manganese (*i.e.* oxygen ligands) is oxidized during the $S_2$ to $S_3$ state transition. This conclusion was supported by results from x-ray $K\beta_{1,3}$ emission spectroscopy, which probes the occupied orbitals through 3d-3p exchange interactions and therefore is less affected by the ligand environment (34). The $K\beta_{1,3}$ peak shift was smaller in the $S_2$ to $S_3$ state transition

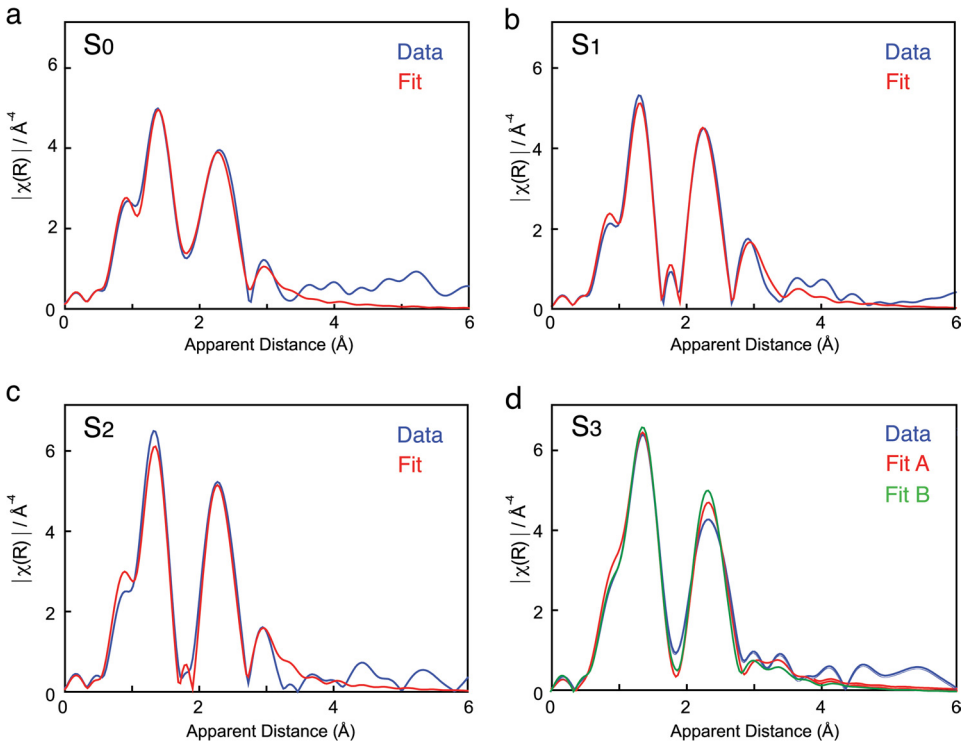


FIGURE 5. **Manganese EXAFS curve fitting results of dimeric PSIIcc solution in $S_0$ to $S_3$ states.** Manganese EXAFS curve fitting results for dimeric PSIIcc solution in $S_0$ (*a*), $S_1$ (*b*), $S_2$ (*c*), and $S_3$ (*d*) states. Only the best fit results are shown in the figure. The details of the fitting parameters are summarized in Table 2. The experimental data are shown in *blue* and the fit data in *red* (and *green*).

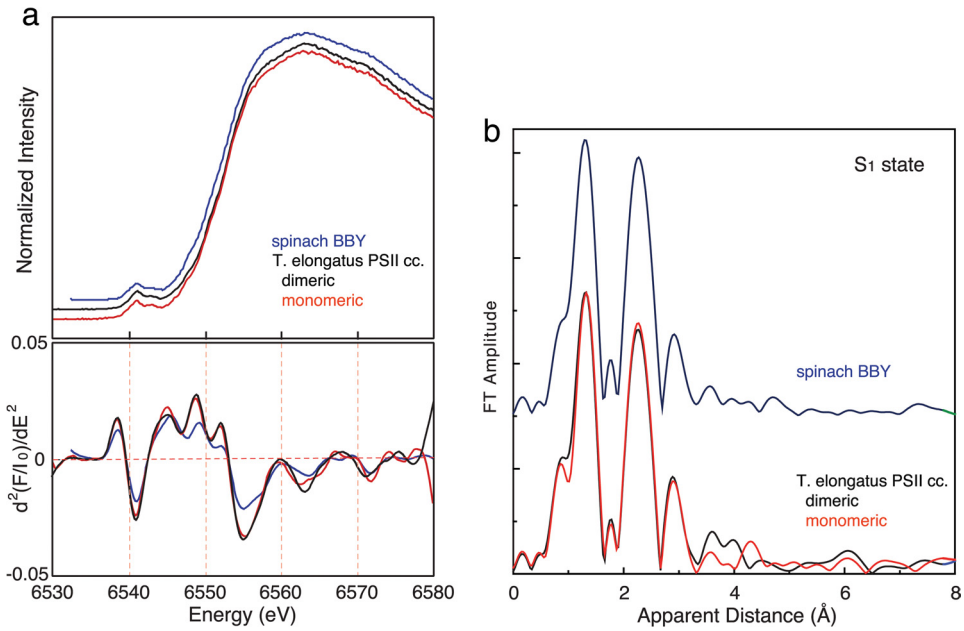


FIGURE 6. **XAS spectra of monomeric and dimeric PSIIcc solution compared with spinach PSII thylakoid membrane fragments.** A comparison of the $S_1$ state manganese XANES spectra (*a*) and their FT spectra (*b*) of monomeric (*red line*) and dimeric (*black line*) PSIIcc solution and spinach PSII thylakoid membrane fragments (*blue line*) is shown.

as compared with the $S_0$ to $S_1$ and $S_1$ to $S_2$ state transitions. However, it is worth noting that the XANES edge shape changes and edge shift could be more complicated when the transition is accompanied by structural changes. Haumann *et al.* (10) showed that the small edge shift and the shape change could occur when one manganese coordination state changes from five to six. A similar change has been proposed by Siegbahn (35), in which an oxygen binds to a five coordinated manganese during the $S_2$ to $S_3$ state transition. As shown under "Results," the structural changes observed in the $S_2$ to $S_3$ state transition are more substantial compared with other S state transitions. Understanding the nature of the electronic structural changes in the $S_2$ to $S_3$ transition may therefore require a more complete understanding of the $S_2$ and the $S_3$ states.

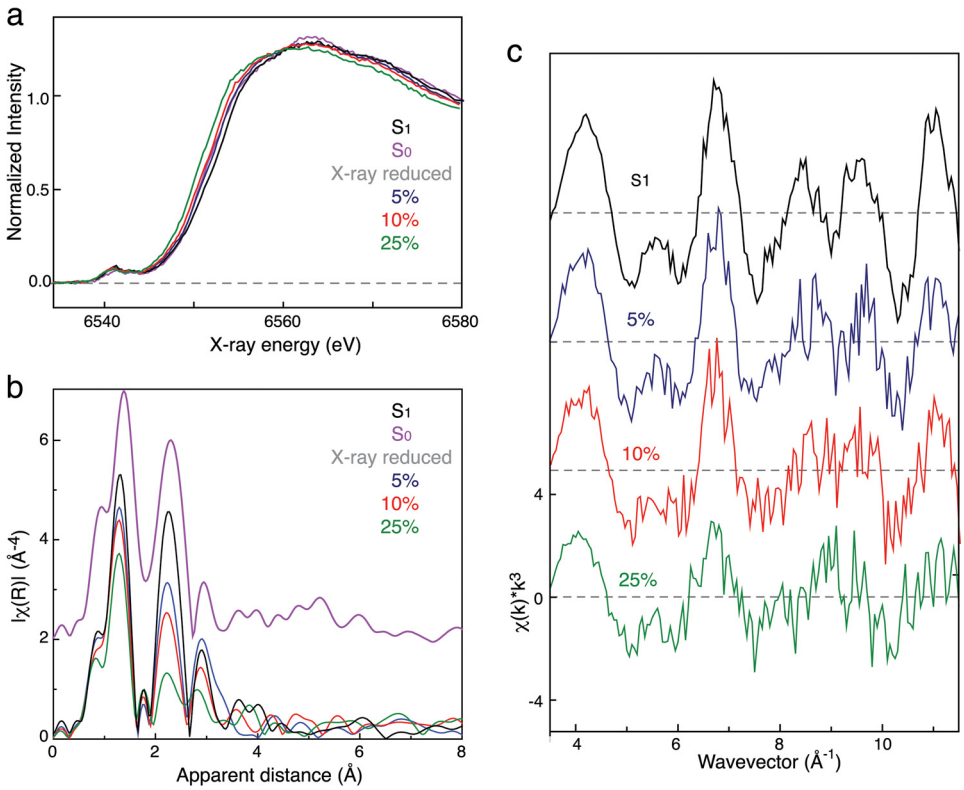


FIGURE 7. **XAS spectra of dimeric PSIIcc solution sample with 0, 5, 10, and 25% reduced Mn.** A comparison of the intact PSIIcc sample in the $S_1$ and $S_0$ states with PSIIcc samples that are 5, 10, and 25% damaged by exposure to x-rays is depicted: *a,* XANES; *b,* Fourier transforms of manganese EXAFS spectra, and *c,* $k^3$-EXAFS spectra. Spectra in *b* and *c* are shown in the same scale, respectively, but with vertical offsets.

**TABLE 3**

**EXAFS fit table for 5, 10, and 25% damaged PSII**

$k$ = 2.4–11.4 (11.5 for 25% damage) ($Å^{-1}$), $E_0$ = 6561.30 eV, $S_0^2$ = 0.85. The boldface letters show the fixed parameters.

| | 5% damage | | | 10% damage | | | 25% damage | | |
|---|---|---|---|---|---|---|---|---|---|
| Path | R | N | $\sigma^2$ | R | N | $\sigma^2$ | R | N | $\sigma^2$ |
| MnO | 1.85 | 3.4 | 0.007 | 1.86 | 3.2 | 0.007 | 1.88 | 3.0 | 0.008 |
| MnO/N | 2.03 | 2.6 | 0.012 | 2.09 | 2.8 | 0.014 | 2.12 | 3.0 | 0.017 |
| MnMn | 2.73 | 1.1 | 0.005 | 2.73 | 0.6 | 0.003 | 2.75 | 0.2 | 0.003 |
| MnMn | 3.28 | 1.0 | 0.004 | 3.27 | 1.2 | 0.049 | 3.26 | 1.5 | 0.011 |
| MnCa | 3.61 | **0.75** | 0.010 | 3.61 | **0.75** | 0.010 | 3.61 | **0.75** | 0.030 |
| *R* factor | | 4.2% | | | 4.6% | | | 3.7% | |
| | | $\Delta E = -15.0$ | | | $\Delta E = -14.6$ | | | $\Delta E = -14.2$ | |

*Dark Stable $S_1$ State Structure*—The dark stable $S_1$ state structure has been studied intensely by EXAFS methods as well as XRD crystallography. The 1.9 Å crystal structure has shown that there are three shorter Mn-Mn interactions around 2.8–2.9 Å and one long Mn-Mn interaction around 3.3 Å (1). The manganese-ligand distances are distributed in the range of 1.8 to 2.6 Å, with an average value of 2.2 Å. The presence of short *versus* long Mn-Mn interactions with a 3:1 ratio is in agreement with the various EXAFS studies in the past as well as with this study. However, overall atomic distances are shorter in the EXAFS results, with manganese-ligand interactions at 1.9 Å and Mn-Mn interactions at 2.7–2.8 Å. This discrepancy likely arises from the distance uncertainties in both methods (XRD ~0.19 Å at 1.9 Å resolution, and EXAFS ~0.02 Å) as well as the inherent x-ray damage to manganese in the OEC during the diffraction measurement. The 1.9-Å crystal structure (1) was collected with a x-ray dose that is significantly lower than what was used in the past XRD studies (16, 18–21), and under these conditions around 25% of manganese is expected to be reduced from native Mn(III)/Mn(IV) oxidation state to Mn(II).

To assess the effect of radiation damage in more detail, XANES and EXAFS spectra were collected from dimeric PSIIcc exposed to low levels of x-ray dose that induces a small amount of manganese reduction (Fig. 7). Even at the level of 5–10% manganese reduction, clear changes in the EXAFS spectrum were observed as shown in Fig. 7.

The origin of the elongation of the atomic distances in the crystal structure has been discussed by several groups; one possibility under consideration is that the originally present $S_1$ state is reduced to the $S_0$ state by the x-rays following the catalytic pathway backwards (36). Other possibilities that have been discussed are the presence of pre-$S_0$ states such as $S_{-1}$, $S_{-2}$, and $S_{-3}$ states in the crystal structure based on the observed atomic distances (36, 37). As shown in Fig. 7, the 25% radiation-damaged PSIIcc EXAFS spectrum is substantially different from the intact $S_0$ state spectrum. Also, even the 5–10% x-ray-reduced

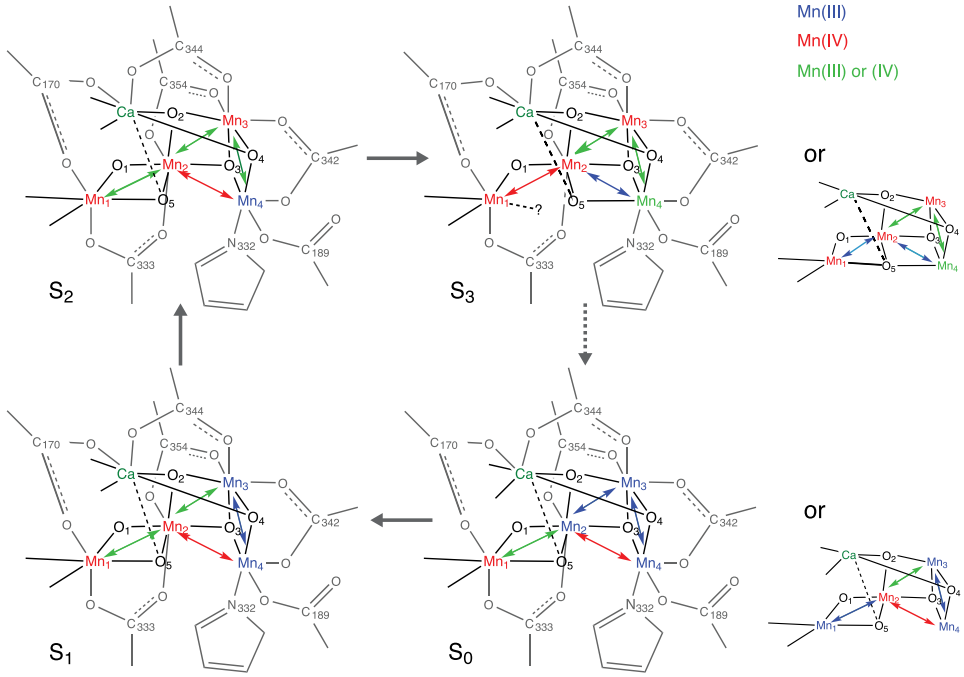


FIGURE 8. **Proposed possible structural changes during the S state transitions.** Possible structural changes during the S state transitions are illustrated. Note that the focus here is to accommodate the EXAFS distance changes, and possible protonation states (at oxo-bridging and terminal water molecules) or changes in the ligand environment (type of ligands and ligation modes) are not included in the figure. The Mn-Mn distances at ~2.7 Å are indicated by *green arrows*, ~2.8 Å by *blue arrows*, and ~3.2 Å by *red arrows*. The *dashed line* indicates that it may not be a bond. For the $S_3$ and the $S_0$ states, two possible models are presented. Manganese atoms are shown in *blue* ($Mn^{III}$), *red* ($Mn^{IV}$), or *magenta* ($Mn^{III}$ or $Mn^{IV}$ possible); calcium is shown in *green*, and the surrounding ligand environment is shown in *gray*.

PSIIcc spectra do not match with the intact $S_1$ state nor the $S_0$ state spectrum (Fig. 7 and Table 3). These findings imply that the reduction of the metal center by x-rays does not go through the catalytic pathway. This is similar to the situation found in the case of Fe/Fe and Fe/Mn ribonucleotide reductase, where the states generated by x-ray photoreduction are significantly different from the native catalytic state of the metal center (38).

*Structural Changes of the $Mn_4CaO_5$ Cluster*—To understand the catalytic mechanism, it is critical to know the distance information within a resolution of 0.1 Å to identify the chemical nature (*e.g.* manganese oxidation state, nature of bridging ligands, and protonation pattern of bridges) of the cluster as well as the detailed structural changes. Such distance changes are expected during the catalytic reaction, accompanied by manganese oxidation state changes as well as proton release. A proton-release pattern of 1:0:1:2 ($S_0$ to $S_1$, $S_1$ to $S_2$, $S_2$ to $S_3$, and $S_3$ to $S_0$) is supported by several studies, including the most recent one using IR spectroscopy (39).

The EXAFS spectra and the curve fitting results of the PSIIcc S states presented in this study show that the structure of the $Mn_4CaO_5$ cluster changes during the catalytic cycle. In particular, the short Mn-Mn interactions undergo distance changes in the range of 2.7 to 2.8 Å.

Such distance changes can reflect several chemical parameters as follows: manganese oxidation state changes, protonation state changes of bridging oxygens, ligation modes (*e.g.* bidentate/monodentate), as well as fundamental changes in geometry (*i.e.* dimeric, trimeric, or cubane-like structure). In the first case, manganese-ligand distances are shortened upon manganese oxidation from Mn(III) to Mn(IV), although Mn-Mn distances within Mn(III)/Mn(IV) and Mn(IV)/Mn(IV) multinuclear complexes strongly depend on the direction of the Jahn-Teller axis (40). When the protonation states of the bridging oxygens are changed, the di-$\mu$-oxo-bridged Mn-Mn distance changes from 2.72 Å (bis-oxo) to 2.84 Å (oxo/hydroxo) and to 2.92 Å (bis-hydroxo) (41). Also, cubane-like structures show generally longer Mn-Mn distances compared with pure bis-$\mu$-oxo dimer complexes (42). Therefore, the observed distance changes could serve as an indicator of the chemical structural changes that occur during the S state transitions.

Possible structural changes of the $Mn_4CaO_5$ cluster during the S state transitions are illustrated in Fig. 8. Our model incorporates the general ligand environment and manganese arrangement found in the 1.9 Å crystal structure (1) but builds upon EXAFS distances, FTIR and EPR results (43–51), and the distance changes extracted from the EXAFS spectra in this work. Among all S states, the $S_2$ state is spectroscopically the most studied state possessing a rich EPR signal (52). Therefore, we consider the S state structural changes starting from our model for the $S_2$ state, described below.

The polarized EXAFS study of single crystals of dimeric PSIIcc (17) supports the open cubane-like structure that was also suggested by Siegbahn (35) for the $S_1$ and $S_2$ states and Neese and co-workers (53) for the $S_2$ state. In the $S_2$ state, a formal oxidation state distribution of $Mn_4$(IV,IV,IV,III) for Mn1,2,3,4 is assumed based on $^{55}$Mn ENDOR measurements (44, 54) and theoretical calculations. In our model, the three short Mn-Mn distances (fitted well to a single shell at 2.74 Å) are assigned to Mn1-Mn2, Mn2-Mn3, and Mn3-Mn4, and the one longer interaction at 3.3 Å to Mn2-Mn4 (Fig. 8).

We observe a distance change in the transition from the dark stable $S_1$ state to the $S_2$ state. This shortening of one Mn-Mn

interaction (~2.79 to ~2.74 Å) is likely due to the oxidation state change of one manganese (formally Mn(III) to Mn(IV)). FTIR difference spectroscopy studies indicated that the manganese atom ligated by Ala-344 undergoes oxidation in the $S_1$ to $S_2$ state transition (55). Accordingly, this oxidation occurs at Mn3 in our model (Fig. 8), in agreement with Mn4 being the Mn(III) moiety in the $S_2$ state as suggested by ENDOR studies on spinach (44) and *T. elongatus* PSII solutions (45) and PSIIcc single crystals (54).

The $S_0$ to $S_1$ state transition is accompanied by the shortening of manganese-ligand distances as well as Mn-Mn distances (~2.8 to ~2.7 Å) (Table 2). The recent EPR/ENDOR studies support the formal oxidation state assignment of $Mn_4(III_3,IV)$ in the $S_0$ state and $Mn_4(III_2,IV_2)$ in the $S_1$ state (43, 56). Therefore, the shortening of the manganese-ligand and Mn-Mn distances could be explained by the elimination of the Jahn-Teller effect at one manganese due to its oxidation. Based on the observed distance changes, we assume the existence of a $Mn(III)_3Ca$ open cubane moiety (accounting for the longer manganese-ligand distances) in the $S_0$ state and Mn2 being the manganese oxidized in the $S_0$ to $S_1$ state transition. Such a $Mn(III)_3$ open cubane moiety can account for the elongation of the manganese-ligand distances observed. Nevertheless, we cannot distinguish between this configuration and the alternative option where the oxidation would take place at Mn1 (shown as *inset* in Fig. 8).

Interestingly, elongations of the Mn-Mn interactions are observed in the $S_2$ to $S_3$ state transition, but not for the $S_0$ to $S_1$ or $S_1$ to $S_2$ state transitions where contractions are observed. This suggests that the $S_2$ to $S_3$ step is not a simple one-oxidation state change of manganese but is accompanied by fundamental changes of the $Mn_4CaO_5$ geometry. Elongation of Mn-Mn due to protonation of an oxo-bridge is unlikely at the $S_2$ to $S_3$ state transition, unless protons from terminal water molecules are transferred to the neighboring bridging oxygens. Instead, we suggest this structural change to be the shift of the oxygen O-5 position from the Mn1 side to the Mn4 side as illustrated in Fig. 8. Such an O-5 shuffling possibility has been suggested by Pantazis and co-workers (48, 49), but as a reason for the change from the $S_2$ low spin ($S = 1/2$) (multiline species) to $S_2$ high spin state ($S = 7/2$) ($g = 4$ species for spinach and $g = 6–10$ for *T. elongatus*), and by Isobe *et al.* (57) in the $S_2$ to $S_3$ state transition using density functional theory calculations. If the oxygen O-5 moves toward the $Mn_3Ca$ open cubane site, a $Mn_3CaO_4$ closed cubane is formed in the $S_3$ state.

Thus far, Mn/Ca heteronuclear complexes have been synthesized by Christou and co-workers and Agapie and co-workers (58, 59). The $Mn^{IV}{}_3Ca_2O_4$ structure reported by Mukherjee *et al.* (58) has Mn-Mn interactions within the closed cubane structure with 2.73, 2.76, and 2.86 Å, with an averaged manganese-bridging oxygen distance of 1.86 Å. The $Mn^{IV}{}_3CaO_4$ structure reported by Kanady *et al.* (59) has three Mn-Mn interactions at 2.83–2.84 Å with an averaged manganese-bridging oxygen distance of 1.87 Å. These Mn-Mn distances are longer than what is observed in manganese dimer or trimer model complexes (40) and would resemble the observed elongation of Mn-Mn distance in the $S_2$ to $S_3$ state transition. The repositioning of oxygen O-5 could be accompanied by changes of the ligand symmetry of Mn1, changing from a five to a six coordinate geometry and leading to the 3.26 Å Mn-Mn distance for Mn1-Mn2.

We have considered two possible structural models for the $S_3$ state, if a $Mn_3CaO_4$ closed cubane-like moiety is formed in this state as follows: one with five coordinated Mn1 upon oxygen O-5 shuffling, and the other with six coordinated Mn1 and no oxygen shuffling. In the latter case, the $N$ number for the ~ 2.7 Å Mn-Mn interactions becomes 2, and in the former case it remains 1.5. Although the EXAFS fitting result slightly prefers $n = 1.5$, the result is not conclusive based only on the EXAFS curve fitting (Table 2 and Fig. 5*d*). In the first case ($S_3$ fit A), Mn1 becomes five coordinated upon the $S_2$ to $S_3$ state transition, or a new ligand, either water or carboxylate, needs to be ligated to maintain the coordination of six at Mn1. In the pre-edge region, which is generally sensitive to the ligand symmetry, the intensity tends to increase upon the $S_2$ to $S_3$ state transition. This could suggest Mn1 to be five coordinated but remains an open question at the moment. A detailed pre-edge analysis combined with theoretical calculations may give us an insight into the ligand symmetry changes, and such an approach is underway.

Upon the $S_3$ to $S_0$ state transition via the $S_4$ state, the ~2.7 Å Mn-Mn distances are shortened. This is counterintuitive as the manganese oxidation state changes from the most oxidized form ($S_3$) to the most reduced state ($S_0$). However, such changes could be explained if the $Mn_4CaO_5$ geometry upon the $S_3$ to $S_0$ state transition reverts back to a structure similar to the $S_1$ and $S_2$ states, where the $Mn_3Ca$ moiety shows open cubane-like structures.

Structural changes of the $Mn_4CaO_5$ cluster have also been studied with strontium XAS using strontium-substituted PSII ($Mn_4SrO_5$ cluster) of *T. elongatus*. The Mn-Sr distance changes were observed during the S state transitions (15), with substantial EXAFS spectral changes in the $S_2$ to $S_3$ state transition. This result, together with the current manganese XAS, demonstrates that Ca(Sr) plays an important role during the $S_2$ to $S_3$ state transition. This is in line with the fact that the OEC does not go beyond the $S_2Yz'$ state (60) when calcium (or strontium) is chemically depleted from PSII (61). More recently, calcium-depleted spinach thylakoid membrane samples were used for studying the role of calcium during the water oxidation reaction, and Lohmiller *et al.* (62) showed that the depletion of calcium from the $Mn_4CaO_5$ core does not disturb the overall structure of the $Mn_4$ moiety on the spin state level in the $S_1$ and $S_2$ states, as well as on the geometry level.[6] The fact that calcium can be removed more easily in the $S_3$ state (or that calcium can be more easily exchanged in the higher S states) (63) compared with the $S_1$ and the $S_2$ state, together with the above observations, implies that the Mn-Ca binding modes are changed upon the $S_2$ to $S_3$ state transition.

In addition to the $Mn_4CaO_5$ core structural changes we discussed here, we expect that terminal ligands that come from carboxylates, histidine, and water/hydroxo ligands change during the catalytic states. In general, it is difficult to get detailed

[6] T. Lohmiller, unpublished EXAFS data.

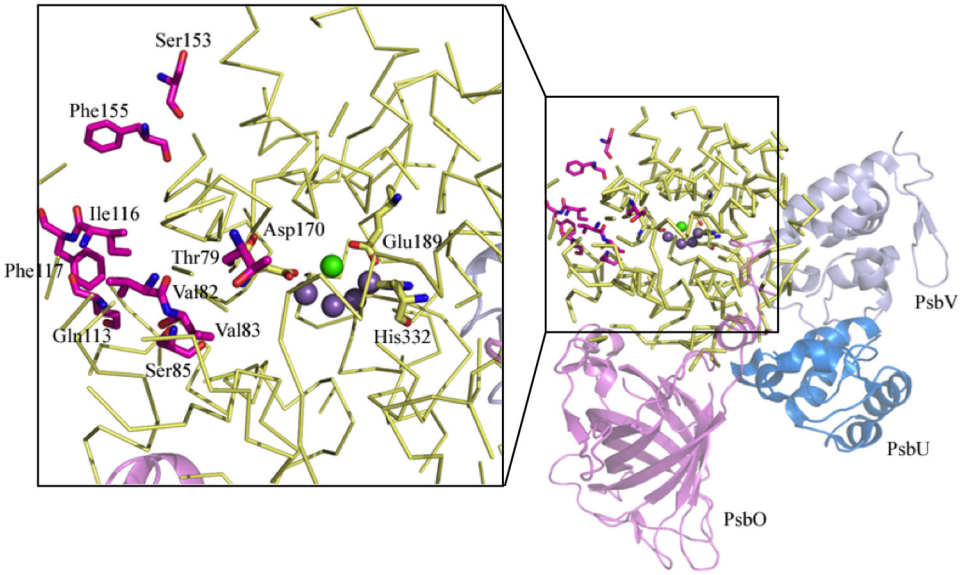


FIGURE 9. **Amino acid residues within a radius of 20 Å around the $Mn_4Ca$ cluster according to the structural model of PSIIcc from *T. elongatus* at 2.9 Å resolution (21).** The *right panel* shows in *yellow* (ribbon mode) the amino acid residues within a radius of 20 Å around the $Mn_4Ca$ cluster (Mn, *purple spheres*; Ca, *green sphere*). Amino acids of subunit D1 different from spinach are highlighted in *pink* and are labeled in the enlarged view on the left (distances are given in supplemental Table S1). For better orientation, the amino acid residues Asp-170, Glu-189, and His-332 (all of subunit D1, *yellow*) are labeled and are shown in *stick mode*. The extrinsic subunits PsbO (*purple*), PsbU (*blue*), and PsbV (*light blue*) are shown in schematic mode. View is of one monomer looking onto the monomer-monomer interface along the membrane plane (tilted by 45° to the left), with the cytoplasm above and the lumen below.

metal-ligand information from EXAFS studies as it only provides averaged distance information. However, it has been shown using site-directed mutant studies that some ligands have critical roles in the OEC activity (5, 64). The replacement of just one His terminal ligand by a glutamate residue (D1-H332E) resulted in a major change in the EXAFS and XANES spectra (64). This illustrates the importance of the ligands in maintaining the active-site structure and how well tuned the active site is by the residues surrounding the $Mn_4CaO_5$ cluster.

*Spinach, Dimeric and Monomeric PSII*—The existence of PSIIcc in both a monomeric and dimeric form has provided the basis for controversial discussions, concerning their contribution to the functionality of the photosynthetic apparatus (65, 66). This discussion in the past included the question whether PSII always exists in a dimeric form, or whether a monomeric PSII is an equally active form. At present, the prevailing view is that the PSII dimer is the fully assembled and functionally relevant form, whereas the monomeric form is seen as an intermediate during the assembly process of all known 20 subunits of PSIIcc and the repair cycle of photo-damaged subunit D1 (67, 68). The assembly of PSII is a stepwise and highly regulated process (69) that includes many auxiliary proteins that are absent in the crystallized complexes. In cyanobacteria, an intermediate Psb27-PSII complex, which has no functional manganese cluster (70), regulates the assembly of the $Mn_4CaO_5$ cluster and the binding of the extrinsic subunits PsbO, PsbU, and PsbV (71) prior to the dimerization of the PSII core complex. Monomerization of photo-damaged PSII was suggested to be triggered by the detachment or structural reorganization of PsbO on the lumenal side (67, 68).

The monomeric form of PSIIcc used in our measurements is obtained in the chromatographic purification procedure of crude PSII extract, together with PSIIcc dimer, as described in Kern *et al.* (23). This purification protocol yields essentially equal amounts of reaction centers in the monomeric and dimeric form. The monomer/dimer ratio from 40 preparations was estimated to be 1.05 ± 0.45 based on the quantity of chlorophyll *a* (22). Moreover, it was shown that the monomeric and dimeric forms of PSIIcc are similar in their oxygen evolving capacity as well as in their subunit content. The crystal structure of monomeric PSIIcc, albeit available at medium resolution so far, gives neither indications of a destabilization of subunit D1 nor a structural reorganization of subunit PsbO.

It is therefore not surprising that the XAS spectra of PSIIcc monomer and dimer are almost identical in the dark stable $S_1$ state (Fig. 6). This comparison provides confidence that the monomeric PSIIcc is suitable for XAS studies and for use in future investigations.

XAS spectra of PSIIcc were also compared with spectra from spinach PSII. Although overall spectral shapes are the same, there are some minor differences observed in the XANES second derivative spectrum (Fig. 6*a*). This is in agreement with the results of Su *et al.* (45) who concluded based on comparison of the $S_2$ multiline and the $S_2$ manganese ENDOR signal from spinach and *T. elongatus* that the electronic structure of the manganese cluster is very similar but not identical between both species.

The alignment of the amino acid sequence of the D1 protein (subunit PsbA) from *T. elongatus* (strain BP-1) and *Spinacia oleracea* (spinach) showed a sequence identity of 84.7% (UniProt). 305 positions are identical and 36 are similar. Within a radius of 20 Å around the OEC, nine amino acid residues are not fully conserved, but eight of them are conserved between groups with strongly similar properties (see Fig. 9 and Table 4). This high conservation makes it unlikely that the slight differences between spinach and *T. elongatus* PSII XAS spectra are due to the differences in the D1 protein. This is also true for subunit CP43 (providing one of the ligands to the $Mn_4CaO_5$

**TABLE 4**

**Shortest distances of amino acid residues, which are different in subunit D1 of PSII from spinach and *T. elongatus*, to the $Mn_4Ca$ cluster**

| Residue in PSIIcc from *T. elongatus* | Residue in PSII from *spinach* | Shortest distance to $Mn_4Ca$ cluster |
|---|---|---|
| | | Å |
| Thr-79 | Ser | 15.4 |
| Val-82 | Ile | 12.4 |
| Val-83 | Ile | 9.8 |
| Ser-85 | Thr | 8.7 |
| Gln-113 | Glu | 14.6 |
| Ile-116 | Val | 14.0 |
| Phe-117 | Leu | 16.7 |
| Ser-153 | Ala | 16.6 |
| Phe-155 | Thr | 15.6 |

cluster) with all residues in the vicinity of the OEC being highly conserved between *T. elongatus* and spinach (data not shown).

The subunit composition of spinach PSII and PSIIcc is slightly different. Although PSIIcc from cyanobacteria has the extrinsic subunits PsbO, PsbU, and PsbV, spinach PSII has neither PsbU nor PsbV but has proteins PsbP and PsbQ instead. The exact localization of PsbP and PsbQ is not yet resolved, but various studies found these two subunits to be important for the stability and activity of the OEC (see Refs. 72–74 and references therein). PsbV and PsbU are found to bind in the vicinity of the OEC with the closest distances to manganese of 11 Å (PsbV-Lys-160) and 14 Å (PsbU-Tyr-133), respectively, and thereby they directly interact with the C terminus of the D1 protein (Fig. 9). Replacing these subunits with PsbP and PsbQ might induce structural changes in the vicinity of the OEC, which could cause the slight variations visible in the XAS spectra, demonstrating the sensitivity of XAS for subtle changes in the electronic structure.

*Conclusion and Outlook*—X-ray absorption spectroscopy results show that the relative position of one of the bridging oxygens in the $Mn_4CaO_5$ cluster may play a critical role in structural changes during the S state transitions and might be involved in the geometric changes of the $Mn_4CaO_5$ cluster during catalysis. This conclusion is crucial for a detailed understanding of the O–O bond formation mechanism during the water oxidation reaction.

Note that more detailed structural changes that could provide evidence, for example, which Mn-Mn distances are shortened/elongated upon S state transition, require orientational information that can be gained from oriented membrane EXAFS or single crystal polarized EXAFS studies. These studies are underway.

*Acknowledgments—We thank Prof. Johannes Messinger for many useful discussions, D. DiFiore for technical assistance with sample preparation and the staff at Stanford Synchrotron Radiation Lightsource, Stanford, CA, for support of the EXAFS measurements. Synchrotron facilities were provided by the Stanford Synchrotron Radiation Lightsource operated by the Department of Energy, Office of Basic Energy Sciences. The Stanford Synchrotron Radiation Lightsource Biomedical Technology program is supported by the National Institutes of Health, the NCCR, and the Department of Energy, Office of Biological and Environmental Research.*

## REFERENCES

1. Umena, Y., Kawakami, K., Shen, J.-R., and Kamiya, N. (2011) Crystal structure of oxygen-evolving photosystem II at a resolution of 1.9 angstrom. *Nature* **473,** 55–60
2. Wydrzynski, T. J., and Satoh, K. (eds) (2005) *Photosystem II: The Light-driven Water:Plastoquinone Oxidoreductase*, Springer, Dordrecht, The Netherlands
3. Kok, B., Forbush, B., and McGloin, M. (1970) Cooperation of charges in photosynthetic oxygen evolution. I. A linear four-step mechanism. *Photochem. Photobiol.* **11,** 457–475
4. Haddy, A. (2007) EPR spectroscopy of the manganese cluster of photosystem II. *Photosynth. Res.* **92,** 357–368
5. Debus, R. J. (2008) Protein ligation of the photosynthetic oxygen-evolving center. *Coord. Chem. Rev.* **252,** 244–258
6. Noguchi, T. (2008) Fourier transform infrared analysis of the photosynthetic oxygen-evolving center. *Coord. Chem. Rev.* **252,** 336–346
7. Sauer, K., Yano, J., and Yachandra, V. K. (2008) X-ray spectroscopy of the photosynthetic oxygen-evolving complex. *Coord. Chem. Rev.* **252,** 318–335
8. Dau, H., and Haumann, M. (2008) The manganese complex of photosystem II in its reaction cycle—Basic framework and possible realization at the atomic level. *Coord. Chem. Rev.* **252,** 273–295
9. Yano, J., and Yachandra, V. K. (2008) Where water is oxidized to dioxygen: Structure of the photosynthetic $Mn_4Ca$ cluster from x-ray spectroscopy. *Inorg. Chem.* **47,** 1711–1726
10. Haumann, M., Müller, C., Liebisch, P., Iuzzolino, L., Dittmer, J., Grabolle, M., Neisius, T., Meyer-Klaucke, W., and Dau, H. (2005) Structural and oxidation state changes of the photosystem II manganese complex in four transitions of the water oxidation cycle ($S_0 \rightarrow S_1$, $S_1 \rightarrow S_2$, $S_2 \rightarrow S_3$, and $S_3$,$S_4 \rightarrow S_0$) characterized by x-ray absorption spectroscopy at 20 K and room temperature. *Biochemistry* **44,** 1894–1908
11. Dau, H., Dittmer, J., Iuzzolino, L., Schiller, H., Dörner, W., Heinze, I., Sole, V. A., and Nolting, H. F. (1997) X-ray absorption linear dichroism spectroscopy (XALDS) on the photosystem II manganese complex: radiation damage and S1-state K-edge spectra. *J. Phys. IV* **7,** 607–610
12. Yano, J., Kern, J., Irrgang, K.-D., Latimer, M. J., Bergmann, U., Glatzel, P., Pushkar, Y., Biesiadka, J., Loll, B., Sauer, K., Messinger, J., Zouni, A., and Yachandra, V. K. (2005) X-ray damage to the $Mn_4Ca$ complex in photosystem II crystals: A case study for metallo-protein x-ray crystallography. *Proc. Natl. Acad. Sci. U.S.A.* **102,** 12047–12052
13. Grabolle, M., Haumann, M., Müller, C., Liebisch, P., and Dau, H. (2006) Rapid loss of structural motifs in the manganese complex of oxygenic photosynthesis by x-ray irradiation at 10–300 K. *J. Biol. Chem.* **281,** 4580–4588
14. Cinco, R. M., Robblee, J. H., Messinger, J., Fernandez, C., McFarlane Holman, K. L., Sauer, K., and Yachandra, V. K. (2004) Orientation of calcium in the $Mn_4Ca$ cluster of the oxygen-evolving complex determined using polarized strontium EXAFS of photosystem II membranes. *Biochemistry* **43,** 13271–13282
15. Pushkar, Y., Yano, J., Sauer, K., Boussac, A., and Yachandra, V. K. (2008) Structural changes in the $Mn_4Ca$ cluster and the mechanism of photosynthetic water splitting. *Proc. Natl. Acad. Sci. U.S.A.* **105,** 1879–1884
16. Loll, B., Kern, J., Saenger, W., Zouni, A., and Biesiadka, J. (2005) Toward complete cofactor arrangement in the 3.0 Å resolution structure of photosystem II. *Nature* **438,** 1040–1044
17. Yano, J., Kern, J., Sauer, K., Latimer, M. J., Pushkar, Y., Biesiadka, J., Loll, B., Saenger, W., Messinger, J., Zouni, A., and Yachandra, V. K. (2006) Where water is oxidized to dioxygen: Structure of the photosynthetic $Mn_4Ca$ cluster. *Science* **314,** 821–825
18. Zouni, A., Witt, H. T., Kern, J., Fromme, P., Krauss, N., Saenger, W., and Orth, P. (2001) Crystal structure of photosystem II from *Synechococcus elongatus* at 3.8 angstrom resolution. *Nature* **409,** 739–743
19. Kamiya, N., and Shen, J. R. (2003) Crystal structure of oxygen-evolving photosystem II from *Thermosynechococcus vulcanus* at 3.7-Å resolution. *Proc. Natl. Acad. Sci. U.S.A.* **100,** 98–103
20. Ferreira, K. N., Iverson, T. M., Maghlaoui, K., Barber, J., and Iwata, S. (2004) Architecture of the photosynthetic oxygen-evolving center. *Science* **303,** 1831–1838
21. Guskov, A., Kern, J., Gabdulkhakov, A., Broser, M., Zouni, A., and Saenger, W. (2009) Cyanobacterial photosystem II at 2.9-angstrom resolution and the role of quinones, lipids, channels and chloride. *Nat. Struct. Mol. Biol.*

**16,** 334–342
22. Broser, M., Gabdulkhakov, A., Kern, J., Guskov, A., Müh, F., Saenger, W., and Zouni, A. (2010) Crystal structure of monomeric photosystem II from *Thermosynechococcus elongatus* at 3.6-Å resolution. *J. Biol. Chem.* **285,** 26255–26262
23. Kern, J., Loll, B., Lüneberg, C., DiFiore, D., Biesiadka, J., Irrgang, K. D., and Zouni, A. (2005) Purification, characterisation and crystallisation of photosystem II from *Thermosynechococcus elongatus* cultivated in a new type of photobioreactor. *Biochim. Biophys. Acta* **1706,** 147–157
24. Messinger, J., Robblee, J. H., Bergmann, U., Fernandez, C., Glatzel, P., Visser, H., Cinco, R. M., McFarlane, K. L., Bellacchio, E., Pizarro, S. A., Cramer, S. P., Sauer, K., Klein, M. P., and Yachandra, V. K. (2001) Absence of Mn-centered oxidation in the $S_2$ to $S_3$ transition: Implications for the mechanism of photosynthetic water oxidation. *J. Am. Chem. Soc.* **123,** 7804–7820
25. Newville, M. (2001) IFEFFIT: Interactive XAFS analysis and FEFF fitting. *J. Synch. Rad.* **8,** 322–324
26. Ravel, B., and Newville, M. (2005) ATHENA, ARTEMIS, HEPHAESTUS: Data analysis for x-ray absorption spectroscopy using IFEFFIT. *J. Synch. Rad.* **12,** 537–541
27. Liang, W., Roelofs, T. A., Cinco, R. M., Rompel, A., Latimer, M. J., Yu, W. O., Sauer, K., Klein, M. P., and Yachandra, V. K. (2000) Structural change of the Mn cluster during the $S_2 \rightarrow S_3$ state transition of the oxygen-evolving complex of photosystem II. Does it reflect the onset of water/substrate oxidation? Determination by Mn X-ray absorption spectroscopy. *J. Am. Chem. Soc.* **122,** 3399–3412
28. Yano, J., Pushkar, Y., Glatzel, P., Lewis, A., Sauer, K., Messinger, J., Bergmann, U., and Yachandra, V. (2005) High-resolution Mn EXAFS of the oxygen-evolving complex in photosystem II: Structural implications for the $Mn_4Ca$ cluster. *J. Am. Chem. Soc.* **127,** 14974–14975
29. Cinco, R. M., McFarlane Holman, K. L., Robblee, J. H., Yano, J., Pizarro, S. A., Bellacchio, E., Sauer, K., and Yachandra, V. K. (2002) Calcium EXAFS establishes the Mn-Ca cluster in the oxygen-evolving complex of photosystem II. *Biochemistry* **41,** 12928–12933
30. Cinco, R. M., Robblee, J. H., Rompel, A., Fernandez, C., Yachandra, V. K., Sauer, K., and Klein, M. P. (1998) Strontium EXAFS reveals the proximity of calcium to the manganese cluster of oxygen-evolving photosystem II. *J. Phys. Chem. B* **102,** 8248–8256
31. Pushkar, Y., Yano, J., Glatzel, P., Messinger, J., Lewis, A., Sauer, K., Bergmann, U., and Yachandra, V. (2007) Structure and orientation of the $Mn_4Ca$ cluster in plant photosystem II membranes studied by polarized range-extended x-ray absorption spectroscopy. *J. Biol. Chem.* **282,** 7198–7208
32. Koua, F. H., Umena, Y., Kawakami, K., and Shen, J. R. (2013) Structure of Sr-substituted photosystem II at 2.1 Å resolution and its implications in the mechanism of water oxidation. *Proc. Natl. Acad. Sci. U.S.A.* **110,** 3889–3894
33. Robblee, J. H., Messinger, J., Cinco, R. M., McFarlane, K. L., Fernandez, C., Pizarro, S. A., Sauer, K., and Yachandra, V. K. (2002) The Mn cluster in the $S_0$ state of the oxygen-evolving complex of photosystem II studied by EXAFS spectroscopy: Are there three di-$\mu$-oxo-bridged $Mn_2$ moieties in the tetranuclear Mn complex? *J. Am. Chem. Soc.* **124,** 7459–7471
34. Pizarro, S. A., Glatzel, P., Visser, H., Robblee, J. H., Christou, G., Bergmann, U., and Yachandra, V. K. (2004) Mn oxidation states in tri- and tetra-nuclear Mn compounds structurally relevant to photosystem II: MnK-edge x-ray absorption and K $\beta$ x-ray emission spectroscopy studies. *Phys. Chem. Chem. Phys.* **6,** 4864–4870
35. Siegbahn, P. E. (2009) Structures and energetics for $O_2$ formation in photosystem II. *Acc. Chem. Res.* **42,** 1871–1880
36. Luber, S., Rivalta, I., Umena, Y., Kawakami, K., Shen, J. R., Kamiya, N., Brudvig, G. W., and Batista, V. S. (2011) $S_1$-state model of the $O_2$-evolving complex of photosystem II. *Biochemistry* **50,** 6308–6311
37. Galstyan, A., Robertazzi, A., and Knapp, E. W. (2012) Oxygen-evolving Mn cluster in photosystem II: The protonation pattern and oxidation state in the high resolution crystal structure. *J. Am. Chem. Soc.* **134,** 7442–7449
38. Sigfridsson, K. G., Chernev, P., Leidel, N., Popovic-Bijelic, A., Gräslund, A., and Haumann, M. (2013) Rapid x-ray photoreduction of dimetal-oxygen cofactors in ribonucleotide reductase. *J. Biol. Chem.* **288,** 9648–9661
39. Suzuki, H., Sugiura, M., and Noguchi, T. (2009) Monitoring proton release during photosynthetic water oxidation in photosystem II by means of isotope-edited infrared spectroscopy. *J. Am. Chem. Soc.* **131,** 7849–7857
40. Mukhopadhyay, S., Mandal, S. K., Bhaduri, S., and Armstrong, W. H. (2004) Manganese clusters with relevance to photosystem II. *Chem. Rev.* **104,** 3981–4026
41. Baldwin, M. J., Stemmler, T. L., Riggs-Gelasco, P. J., Kirk, M. L., Penner-Hahn, J. E., and Pecoraro, V. L. (1994) Structural and magnetic effects of successive protonations of oxo bridges in high valent manganese dimers. *J. Am. Chem. Soc.* **116,** 11349–11356
42. Cinco, R. M., Rompel, A., Visser, H., Aromí, G., Christou, G., Sauer, K., Klein, M. P., and Yachandra, V. K. (1999) Comparison of the manganese cluster in oxygen-evolving photosystem II with distorted cubane manganese compounds through x-ray absorption spectroscopy. *Inorg. Chem.* **38,** 5988–5998
43. Kulik, L. V., Epel, B., Lubitz, W., and Messinger, J. (2007) Electronic structure of the $Mn_4O_x$ Ca cluster in the $S_0$ and $S_2$ states of the oxygen-evolving complex of photosystem II based on pulse $^{55}$Mn-ENDOR and EPR spectroscopy. *J. Am. Chem. Soc.* **129,** 13421–13435
44. Cox, N., Rapatskiy, L., Su, J. H., Pantazis, D. A., Sugiura, M., Kulik, L., Dorlet, P., Rutherford, A. W., Neese, F., Boussac, A., Lubitz, W., and Messinger, J. (2011) Effect of $Ca^{2+}/Sr^{2+}$ substitution on the electronic structure of the oxygen-evolving complex of photosystem II: a combined multifrequency EPR, $^{55}$Mn-ENDOR, and DFT study of the $S_2$ state. *J. Am. Chem. Soc.* **133,** 3635–3648
45. Su, J. H., Cox, N., Ames, W., Pantazis, D. A., Rapatskiy, L., Lohmiller, T., Kulik, L. V., Dorlet, P., Rutherford, A. W., Neese, F., Boussac, A., Lubitz, W., and Messinger, J. (2011) The electronic structures of the $S_2$ states of the oxygen-evolving complexes of photosystem II in plants and cyanobacteria in the presence and absence of methanol. *Biochim. Biophys. Acta* **1807,** 829–840
46. Siegbahn, P. E. (2011) The effect of backbone constraints: the case of water oxidation by the oxygen-evolving complex in PSII. *Chem. Phys. Chem.* **12,** 3274–3280
47. Siegbahn, P. E. (2011) Recent theoretical studies of water oxidation in photosystem II. *J. Photochem. Photobiol. B* **104,** 94–99
48. Pantazis, D. A., Ames, W., Cox, N., Lubitz, W., and Neese, F. (2012) Two interconvertible structures that explain the spectroscopic properties of the oxygen-evolving complex of photosystem II in the $S_2$ state. *Angew. Chem. Int. Ed. Engl.* **51,** 9935–9940
49. Cox, N., Pantazis, D., Neese, F., and Lubitz, W. (March 18, 2013) Biological water oxidation. *Acc. Chem. Res.,* 10.1021/ar3003249
50. Peloquin, J. M., Campbell, K. A., Randall, D. W., Evanchik, M. A., Pecoraro, V. L., Armstrong, W. H., and Britt, R. D. (2000) $^{55}$Mn ENDOR of the $S_2$-state multiline EPR signal of photosystem II: Implications on the structure of the tetranuclear cluster. *J. Am. Chem. Soc.* **122,** 10926–10942
51. Peloquin, J. M., and Britt, R. D. (2001) EPR/ENDOR characterization of the physical and electronic structure of the OEC Mn cluster. *Biochim. Biophys. Acta* **1503,** 96–111
52. Dismukes, G. C., and Siderer, Y. (1981) Intermediates of a polynuclear manganese cluster involved in photosynthetic oxidation of water. *Proc. Natl. Acad. Sci. U.S.A.* **78,** 274–278
53. Ames, W., Pantazis, D. A., Krewald, V., Cox, N., Messinger, J., Lubitz, W., and Neese, F. (2011) Theoretical evaluation of structural models of the $S_2$ state in the oxygen evolving complex of photosystem II: Protonation states and magnetic interactions. *J. Am. Chem. Soc.* **133,** 19743–19757
54. Teutloff, C., Pudollek, S., Kessen, S., Broser, M., Zouni, A., and Bittl, R. (2009) Electronic structure of the tyrosine D radical and the water-splitting complex from pulsed ENDOR spectroscopy on photosystem II single crystals. *Phys. Chem. Chem. Phys.* **11,** 6715–6726
55. Chu, H. A., Hillier, W., and Debus, R. J. (2004) Evidence that the C terminus of the D1 polypeptide of photosystem II is ligated to the manganese ion that undergoes oxidation during the $S_1$ to $S_2$ transition: An isotope-edited FTIR study. *Biochemistry* **43,** 3152–3166
56. Kulik, L. V., Epel, B., Lubitz, W., and Messinger, J. (2005) $^{55}$Mn pulse ENDOR at 34 GHz of the $S_0$ and $S_2$ states of the oxygen-evolving complex in photosystem II. *J. Am. Chem. Soc.* **127,** 2392–2393
57. Isobe, H., Shoji, M., Yamanaka, S., Umena, Y., Kawakami, K., Kamiya, N.,

Shen, J. R., and Yamaguchi, K. (2012) Theoretical illumination of water-inserted structures of the $CaMn_4O_5$ cluster in the $S_2$ and $S_3$ states of oxygen-evolving complex of photosystem II: full geometry optimizations by B3LYP hybrid density functional. *Dalton Trans.* **41,** 13727–13740

58. Mukherjee, S., Stull, J. A., Yano, J., Stamatatos, T. C., Pringouri, K., Stich, T. A., Abboud, K. A., Britt, R. D., Yachandra, V. K., and Christou, G. (2012) Synthetic model of the asymmetric $Mn_3CaO_4$ cubane core of the oxygen-evolving complex of photosystem II. *Proc. Natl. Acad. Sci. U.S.A.* **109,** 2257–2262
59. Kanady, J. S., Tsui, E. Y., Day, M. W., and Agapie, T. (2011) A synthetic model of the $Mn_3Ca$ subsite of the oxygen-evolving complex in photosystem II. *Science* **333,** 733–736
60. Boussac, A., Zimmermann, J.-L., and Rutherford, A. W. (1989) EPR signals from modified charge accumulation states of the oxygen evolving enzyme in $Ca^{2+}$-deficient photosystem II. *Biochemistry* **28,** 8984–8989
61. Ono, T., and Inoue, Y. (1988) Discrete extraction of the Ca atom functional for $O_2$ evolution in higher-plant photosystem II by a simple low pH treatment. *FEBS Lett.* **227,** 147–152
62. Lohmiller, T., Cox, N., Su, J. H., Messinger, J., and Lubitz, W. (2012) The basic properties of the electronic structure of the oxygen-evolving complex of photosystem II are not perturbed by $Ca^{2+}$ removal. *J. Biol. Chem.* **287,** 24721–24733
63. Miqyass, M., van Gorkom, H. J., and Yocum, C. F. (2007) The PSII calcium site revisited. *Photosynth. Res.* **92,** 275–287
64. Yano, J., Walker, L. M., Strickler, M. A., Service, R. J., Yachandra, V. K., and Debus, R. J. (2011) Altered structure of the $Mn_4Ca$ cluster in the oxygen-evolving complex of photosystem II by a histidine ligand mutation. *J. Biol. Chem.* **286,** 9257–9267
65. Watanabe, M., Iwai, M., Narikawa, R., and Ikeuchi, M. (2009) Is the photosystem II complex a monomer or a dimer? *Plant Cell Physiol.* **50,** 1674–1680
66. Takahashi, T., Inoue-Kashino, N., Ozawa, S., Takahashi, Y., Kashino, Y., and Satoh, K. (2009) Photosystem II complex *in vivo* is a monomer. *J. Biol. Chem.* **284,** 15598–15606
67. Nixon, P. J., Michoux, F., Yu, J., Boehm, M., and Komenda, J. (2010) Recent advances in understanding the assembly and repair of photosystem II. *Ann. Bot.* **106,** 1–16
68. Komenda, J., Sobotka, R., and Nixon, P. J. (2012) Assembling and maintaining the photosystem II complex in chloroplasts and cyanobacteria. *Curr. Opin. Plant Biol.* **15,** 245–251
69. Komenda, J., Reisinger, V., Müller, B. C., Dobáková, M., Granvogl, B., and Eichacker, L. A. (2004) Accumulation of the D2 protein is a key regulatory step for assembly of the photosystem II reaction center complex in *Synechocystis* PCC 6803. *J. Biol. Chem.* **279,** 48620–48629
70. Nowaczyk, M. M., Hebeler, R., Schlodder, E., Meyer, H. E., Warscheid, B., and Rögner, M. (2006) Psb27, a cyanobacterial lipoprotein, is involved in the repair cycle of photosystem II. *Plant Cell* **18,** 3121–3131
71. Roose, J. L., and Pakrasi, H. B. (2008) The Psb27 protein facilitates manganese cluster assembly in photosystem II. *J. Biol. Chem.* **283,** 4044–4050
72. Ifuku, K., Ido, K., and Sato, F. (2011) Molecular functions of PsbP and PsbQ proteins in the photosystem II supercomplex. *J. Photochem. Photobiol. B* **104,** 158–164
73. Kouřil, R., Dekker, J. P., and Boekema, E. J. (2012) Supramolecular organization of photosystem II in green plants. *Biochim. Biophys. Acta* **1817,** 2–12
74. Bricker, T. M., Roose, J. L., Fagerlund, R. D., Frankel, L. K., and Eaton-Rye, J. J. (2012) The extrinsic proteins of Photosystem II. *Biochim. Biophys. Acta* **1817,** 121–142